A THz Integrated Circuit based on a Pixel Array to Mode Multiplex Two 10-Gbit/s QPSK Channels Each on a Different OAM Beam

Xinzhou Su, Hao Song, Huibin Zhou, Kaiheng Zou, Yuxiang Duan, Narek Karapetyan, Runzhou Zhang, Amir Minoofar, Haoqian Song, Kai Pang, Shlomo Zach, Andreas F. Molisch, *Fellow, IEEE,* Moshe Tur, *Life Fellow, IEEE, Fellow, OSA*, and Alan E. Willner, *Fellow, IEEE, Fellow, OSA*

(Post-Deadline Paper)

Abstract*—We experimentally demonstrate a THz integrated circuit with a pixel-array-based orbital-angular-momentum (OAM) mode converter for the generation and multiplexing of multiple data-carrying OAM beams. The integrated device consists of (i) two coupling spikes, which serve as inputs and can couple THz signals from hollow metallic waveguides to the device; (ii) two mode expansion structures, which expand the mode profiles from the waveguide inputs to match the OAM mode converter; and (iii) a 3.6 × 3.6 mm^2 pixel-array-based OAM mode converter, which vertically emits and multiplexes two free-space THz data-carrying OAM beams with different mode orders. The generated OAM order depends on the corresponding input port. Two different designs of the integrated OAM emitters show the generation and multiplexing of (a) OAM +1 and –1, and (b) OAM +1 and –2 at the center frequency of ~ 0.317 THz. Crosstalk lower than –15 dB between the OAM modes can be achieved. Specifically, the OAM +1/–1 emitter has a 3-dB power bandwidth of ~15 GHz. Using the OAM +1/–1 emitter for a free-space link at a 0.317-THz carrier frequency, we experimentally demonstrate 20-Gbit/s quadrature-phase-shift-keying (QPSK) transmission by multiplexing OAM +1 and –1. Compared to a single-beam transmission, the multiplexed link induces a ~1-dB signal-to-noise ratio (SNR) penalty at the bit error rate (BER) of 3.8×10^{-3}.

***Index Terms*—Orbital angular momentum, mode-division-multiplexing, terahertz communication.**

I. Introduction

TERAHERTZ (THz) free-space communication systems are gaining interest due to their (a) higher spectral bandwidth and lower beam divergence when compared to millimeter waves [1], and (b) lower beam degradation due to atmospheric turbulence when compared to optical waves [2], [3]. In particular, the spectral band in the 300-GHz carrier wave frequency region is low in atmospheric absorption and turbulence effects [2].

Taking advantage of these issues, several demonstrations have been reported of free-space THz communication links that transmit a single Gaussian beam from the transmitter to the receiver [4]–[11]. Interestingly, THz communications have garnered interest for potential deployment in ultra-high data rate communications for wireless local-area networks (WLANs) (where the IEEE 802.15.3d standard has been established) and 6G systems [12], [13].

Similar to communication systems in other frequency ranges, there have been advances in THz links to increase system capacity by multiplexing multiple independent data-carrying beams at the transmitter, transmitting them over the same free-space medium, and demultiplexing them at the receiver. Examples of capacity enhancement using channel multiplexing include frequency- and polarization-division multiplexing [5], [6].

An additional multiplexing domain is space-division-multiplexing (SDM), which can be compatible with the other multiplexing techniques. A subset of SDM is mode-division-multiplexing (MDM), in which each THz beam has a different spatial modal structure that is orthogonal to all other beams [14]–[16]. One example of a modal basis set is orbital-angular-momentum (OAM), which is a subset of Laguerre Gaussian (LG) modes [16]–[18]. Each beam has (i) a different OAM ℓ

This work was supported in part by Vannevar Bush Faculty Fellowship sponsored by the Basic Research Office of the Assistant Secretary of Defense (ASD) for Research and Engineering (R&E) and funded by the Office of Naval Research under Grant N00014-16-1-2813, in part by the Defense Security Cooperation Agency (DSCA) under Grant 4440646262, in part by the Airbus Institute for Engineering Research, in part by the Defense University Research Instrumentation Program (DURIP) under Grant FA9550-20-1-0152, in part by the Air Force Office of Scientific Research (subaward of FA9453-20-2-0001), and in part by Qualcomm Innovation Fellowship (QIF). *(Corresponding author: Xinzhou Su.)*

Xinzhou Su, Hao Song, Huibin Zhou, Kaiheng Zou, Yuxiang Duan, Narek Karapetyan, Runzhou Zhang, Amir Minoofar, Haoqian Song, Kai Pang, and Andreas F. Molisch are with the Ming Hsieh Department of Electrical and Computer Engineering, University of Southern California, Los Angeles, CA 90089 USA (e-mail: xinzhous@usc.edu; songhao@usc.edu; huibinzh@usc.edu; kaihengz@usc.edu; yuxiangd@usc.edu; narekkar@usc.edu; runzhou@usc.edu; minoofar@usc.edu; haoqians@usc.edu; kaipang@usc.edu; molisch@usc.edu).

Shlomo Zach and Moshe Tur are with the School of Electrical Engineering, Tel Aviv University, Ramat Aviv 69978, Israel (e-mail: szach1@gmail.com; tur@post.tau.ac.il).

Alan E. Willner is with the Ming Hsieh Department of Electrical and Computer Engineering, and Joint Appointment with Dornsife Department of Physics and Astronomy, University of Southern California, Los Angeles, CA 90089 USA (e-mail: willner@usc.edu).

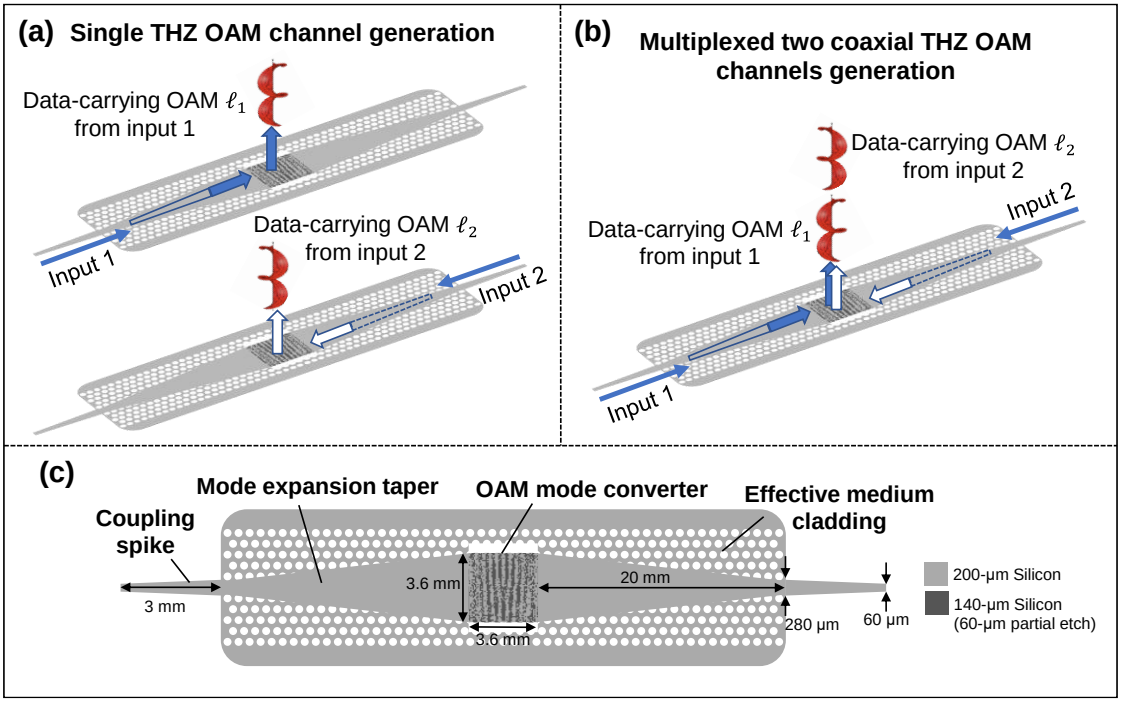

Fig. 1. Concept of pixel-array-based THz integrated OAM emitter (a) to generate a single data-carrying THz OAM beam and (b) to generate two coaxially multiplexed data-carrying THz OAM beams. (c) Schematic diagram of the integrated OAM emitter. The device is made from a 200-µm thick silicon slab with 60-µm partially etched pattern. The mode converter for OAM +1 and –1 is shown in the diagram as an example.

value, which is the number of 2π phase changes in the azimuthal direction; and (ii) a donut-shaped intensity profile [17], [18].

As is the case in general, terminal devices for multiple data channels can significantly benefit from integration in terms of reducing size and cost. Such advances were reported for optical communications using photonic integrated circuits (PIC) [19], [20]. Likewise, integrated circuits would potentially bring significant value to THz communication systems [20]–[23]. In terms of OAM in the THz region, reports of integration include: (a) a metasurface that converts a free-space Gaussian beam into a free-space OAM beam [24]–[27], and (b) an integrated circuit that generates a single OAM beam with tunable mode order into free space, such that each bit is encoded on different OAM modes at ~Mbit/s [28]. A laudable goal might be to demonstrate a THz integrated circuit (TIC) that generates multiple >Gbit/s OAM beams and multiplexes them together for transmission [29].

In this paper, we experimentally demonstrate a TIC based on a pixel array that multiplexes two 10-Gbit/s quadrature-phase-shift-keying (QPSK) channels, each on a different OAM beam, for an MDM link. We design and fabricate two different THz integrated OAM emitters for the generation and multiplexing of two OAM beams, one for a +1/–1 mode combination and one for a +1/–2 combination. The OAM emitters are designed to have pixel array antennas that can vertically emit and multiplex free-space THz data-carrying OAM beams with signals coupled from hollow metallic waveguides. For both emitters, the crosstalk between the two modes is less than –15 dB at the center frequency of 0.317 THz. The OAM +1/-1 device has a 3-dB power bandwidth of ~15 GHz, and the crosstalk is < –10 dB within this band. Using this +1/-1 TIC, we experimentally demonstrate a 20-Gbit/s QPSK 25-cm free-space THz link at 0.317 THz by multiplexing OAM +1 and –1 modes. Compared to a single-beam transmission, the multiplexed link induces ~1-dB signal-to-noise ratio (SNR) penalties.

We note that this manuscript is an extension of our previous OFC summary paper [29] by providing additional background information, concepts, technical details, and experimental results. For example, in this contribution, we include a detailed explanation of the THz integrated OAM emitter, such as basic concepts and design principles. Moreover, we also demonstrate another example of an integrated OAM emitter with a different modal set for multiplexing OAM +1 and –2.

II. Concept and Fabrication Results

Figure 1 shows the concept of a pixel-array-based THz integrated OAM emitter. This device is made of a single-layer silicon slab with a partially etched pattern. The THz integrated OAM emitter has two input ports that can be inserted into the hollow metallic waveguides, and couple data-carrying THz signals from the metallic waveguides to the silicon slab. To generate the OAM beams, as shown in Fig. 1(a), the OAM mode converter at the center of the device is designed to vertically couple input THz waveguide mode into a free-space OAM beam. The integrated OAM emitter can be designed so that generated OAM beams from different input ports have different OAM orders, the same linear polarization, and coaxial propagation directions in free space. Consequently, multiplexing of two coaxially propagated data-carrying OAM channels can be achieved, as shown in Fig. 1(b). We note that the device is designed to be a THz OAM generator and multiplexer. However, as a passive reciprocal device, the THz integrated OAM emitter could also be used as an OAM receiver (*e.g.*, demultiplexing two coaxially propagated OAM beams

and convert them back to two THz waveguide modes at different TIC ports) [30].

A. Design of the THz-integrated OAM emitter

The schematic diagram of the THz integrated OAM emitter with a center frequency ~0.315 THz is illustrated in Fig.1 (c). The device consists mainly of three regions: (i) two coupling spikes as input ports; (ii) two mode expansion structures made of adiabatic tapers surrounded by effective medium cladding, the effective medium can function as the low-refractive-index cladding and mechanical supporting frame of the device [31]; and (iii) a 3.6 × 3.6 mm^2 pixel-array-based OAM mode converter that can vertically multiplex and emit two data-carrying OAM channels. The structures are designed and simulated using the Lumerical finite-difference time-domain (FDTD) simulation.

The device is fabricated from high-resistivity float-zone intrinsic silicon wafers with resistivity of > 20 kΩ·cm and 200 μm thickness. This type of single-layer silicon slab has been reported to provide low-loss signal transmission of sub-THz waves [22], [31]. The relative permittivity ϵ_{si} is estimated to be 11.68 for the design and simulation, resulting in a refractive index of $n_{si} = \sqrt{\epsilon_{si}} = 3.417$. The pixel-array-based OAM converter at the center of the device has a designed pattern that is partially etched with a 60-μm depth. The rest of the structure and the whole device are fully etched and are subsequently removed from the wafers.

1) Coupling spike

The coupling spikes are designed to couple the THz signal power from the WR3.4 hollow metallic waveguides to the silicon waveguides. Typically, WR3.4 waveguides have a standard internal size of 864 μm (height) × 432 μm (width), and support a single fundamental transverse-electric (TE) mode. In our design, the coupling spike has a trapezoid shape with widths of 60 μm and 280 μm, and a length of 3 mm. The simulation results show a coupling loss of 0.07 dB from the hollow metallic waveguides to the silicon waveguides. The actual coupling loss is also characterized as negligible by utilizing a device with only two coupling spikes and straight waveguides. We note that coupling spikes are not necessary for integrated OAM emitter designs. For an integrated THz system, the mode converter could potentially be directly connected and integrated with other components, such as the THz source and receiver [22].

2) Mode expansion structure

Since the width of the coupling spike waveguide is 280 μm, while that of the OAM emitter is 3.6 mm, a mode expander is designed to match the modal profile. The mode expansion structure consists of an adiabatic taper surrounded by effective medium cladding. The adiabatic taper is designed to be a simple linear tapering structure with a trapezoid shape. The taper has a length of 20 mm, with the waveguide width expanding from 280 μm to 3.6 mm. The effective medium is designed to be a periodic dense hollow lattice. The relative permittivity of the effective medium is estimated by the Maxwell-Garnett approximation [22], [31] to be:

$$\epsilon_{eff} = n_{eff}^2 = \epsilon_{si}\frac{(\epsilon_0 + \epsilon_{si}) + (\epsilon_0 - \epsilon_{si})\zeta_d}{(\epsilon_0 + \epsilon_{si}) - (\epsilon_0 - \epsilon_{si})\zeta_d}, \quad (1)$$

where ϵ_0 and ϵ_{si} are the relative permittivities of air and silicon, respectively, and ζ represents the fill factor of the air in silicon. The value of the filling factor is dependent on the pattern of the array of holes. For a hexagonal lattice, the filling factors can be calculated as $\pi d^2/(2\sqrt{3}a^2)$, where d is the hole diameter, and a is the lattice constant, *i.e.*, the distance between the centers of two adjacent holes. In our design, we select d = 110 μm and a = 120 μm, thus, ζ_d = 0.76, and the index of the effective medium is estimated to be 1.6.

Based on this design, we simulate the modal profile after the tapering structure, and calculated the mode purity of the fundamental TE mode by the double integral $\left|\iint E_{taper}E_{TE}^*\right|^2$, where E_{taper} is the normalized electrical field of the expanded mode after the taper, and E_{TE} is the normalized fundamental TE mode. Figure 2(a) presents the THz fields in the taper waveguide at the positions of the input, middle of the structure, and output. The simulation results show a fundamental TE modal purity of 97.5% at the output after expansion. The simulated THz field expansion along the taper is shown in Fig 2(b). For simplicity, we used a linear tapering structure in our demonstration. The footprint of the taper structure could potentially be reduced by utilizing similar designs for photonic integrated circuits.

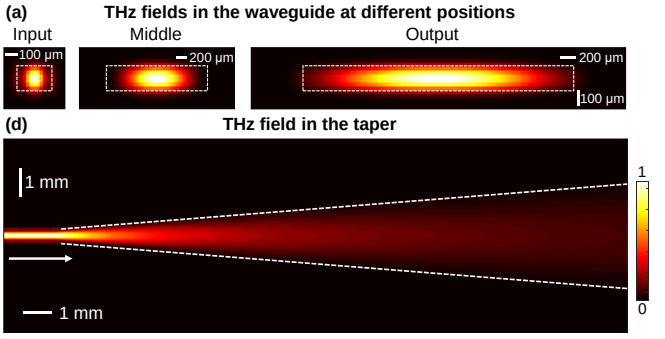

Fig. 2. (a) Simulated THz field in the taper waveguide at the input, middle of the structure, and output. (b) Simulated THz field expansion in the tapering structure.

3) Pixel-array-based OAM converter

A pixel-array-based mode converter is used as an OAM emitter in our design. The concept of the mode converter is illustrated in Fig. 3(a). The phase profile of the vertically emitted beam at different locations is jointly controlled by the propagating path length and different pixels at different locations. In general, the resulting phase delay at each location $\phi(x, y)$ is composed of both the propagation-induced phase ϕ_1 and the pixel-induced phase ϕ_2 (the pixel type is determined by the area with or without a partial etch). Each pixel in the mode converter has a sub-wavelength pixel size and etching depth. To design the pixel-array-based OAM mode converter, the generated phase profiles from the left port (ϕ_{left}) and right port (ϕ_{right}) are required to be as follows [30]:

$$\begin{cases} \phi_{left} = \phi_{1_{left}} + \phi_{2_{left}} = \ell_{left}\theta \\ \phi_{right} = \phi_{1_{right}} + \phi_{2_{right}} = \ell_{right}\theta \end{cases}, \quad (2)$$

where ℓ_{left} and ℓ_{right} are the mode orders of the generated OAM modes from the left and right ports, respectively, and θ

represents the azimuthal angle. Subsequently, the generated modes with inputs from the left and right ports will have different azimuthal 2π phase changes, leading to different OAM orders. However, the analytical solution to these equations is difficult to obtain. Alternatively, we utilize an optimization algorithm to design the distribution of the pixels to jointly control the THz spatial phase profiles [30], [32]. We note that the pixel-array-based mode converter shares a similar concept with the multiplexing metasurface. By controlling the phase using sub-wavelength structures, different input Gaussian beams with different incident angles or polarization onto the metasurface could be converted to co-axial OAM beams with different OAM orders [33]–[35].

In general, the modal quality of the generated OAM beam is determined by the phase shift accuracy of the generated beam. In our case, the phase difference between the designed pattern and the theoretical helical phasefront would be globally dependent on the optimization results. Nevertheless, structure parameters (e.g., the size of the mode converter area, the size of each pixel, and etching depth) can lead to different optimization results, and influence the generated modal purity. In terms of size, a larger emitting area would support higher-order OAM modes, and a smaller pixel size would increase the spatial resolution of the phase profiles [36]. However, there might be a trade-off between optimization complexity and the number of pixels in the structure. Other optimization methods, such as inverse design, might also help with this problem [37]–[40]. In terms of etching depth, since the partial etch creates the pixel-induced phase ϕ_2, the difference in the etching depth would influence the modal purity and the center frequency of the device [41]. In addition, the etching depth affects the emission efficiency, so it would also have an influence on the mode conversion efficiency [41].

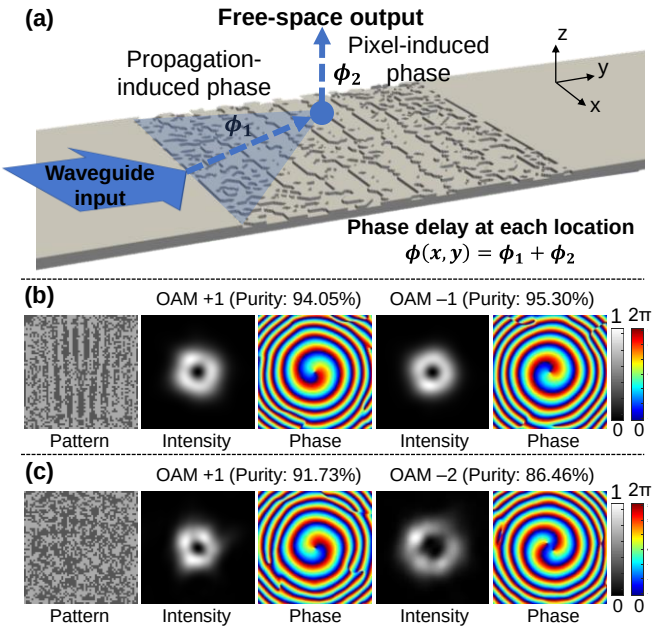

Fig. 3. (a) Concept of an OAM mode converter that vertically emits different spatial modes from different waveguide inputs. Simulated far-field intensity and phase profiles of (b) the mode converter design for OAM +1 and –1, and (c) the mode converter design for OAM +1 and –2.

In our design, we iteratively use a direct binary search algorithm to optimize the OAM emitter [32]. In each iteration step, we excite the two waveguide inputs with fundamental TE modes and capture the output field at the top of the pixel-array-based mode convertor. Given the normalized output field of the generated mode E_{output}, the corresponding modal purity C_ℓ is calculated as

$$C_\ell = \left| \iint E_{output} E^*_{OAM\,\ell} \right|^2, \tag{3}$$

where $E_{OAM\,\ell}$ is the normalized ideal OAM field with an order of ℓ. Subsequently, we iteratively improve the performance of the OAM emitter by randomly switching the state of the pixels one at a time, and maximizing the OAM modal purity on the designed mode for each input port, while minimizing the modal purity of the mode for the other input port (*i.e.*, minimizing modal crosstalk).

The designed OAM mode converter has a footprint of 3.6 × 3.6 mm^2. The pixel array is composed of 3600 (60 × 60) pixels in total, each of which has a size of 60 × 60 μm^2. The etch depth is designed to be 60 μm. We optimize the polarization of the generated OAM beam to be along the y-axis. We have investigated mode converters for OAM +1/–1 (with the same absolute but opposite value of mode orders) and OAM +1/–2 (with different absolute values of mode orders) as two examples. For the OAM +1/–2 mode converter, the pixel array pattern is initialized with a random distribution to ensure a large search space for the optimization process. For the OAM +1/–1 mode converter, it is initialized with a fork-grating pattern. We note that the fork-grating pattern can be used as a theoretical solution to generate OAM modes with opposite OAM orders [41]. In this case, iterative optimization can help to further improve the beam quality of the generated modes in terms of modal purity and conversion efficiency. For modal sets that have theoretical pattern solutions or approximations (e.g., opposite OAM orders), using the theoretical pattern as the initialization might reduce the calculation complexity and enhance the efficiency of the optimization process [30].

The optimized pattern design and simulated far-field intensity and phase profiles of the two OAM converters (*e.g.*, OAM +1/–1, and OAM +1/–2) are shown in Figs. 3(b) and (c), respectively. For OAM –2, the modal purity tends to be lower. This could be due to multiple reasons mentioned before.

In our work, the proposed OAM converter can generate and multiplex two OAM beams with fixed OAM orders (+1/–1 or +1/–2) on a linear polarization. It might also be possible to generate higher-order OAM modes and multiplex more modes. To achieve this, a larger mode converter area with a smaller pixel size would likely be required to capture the larger modal fields of higher-order modes [36]. This might require extra optimization and fabrication complexity. Furthermore, more inputs might be supported by specially designed couplers to the mode converter with more input waveguides (e.g., MMI or star coupler) [42], [43]. The generated OAM mode order could be tuned with an added phase shifter at each input port [44]. Meanwhile, the OAM converter might also be potentially designed for dual-polarization mode multiplexing with input

excitation from both directions of the mode converter [41]. Moreover, we mainly focus on the integrated OAM emitter, which is for a one-dimensional modal set, but we believe that the general approach could be applicable for LG beams with variations in both azimuthal and radial dimensions [45]. It might also be suitable for supporting other mode bases sets, *e.g.*, Hermite-Gaussian (HG) modes or linear polarized (LP) modes [46]–[48].

B. Fabrication results

The fabrication is based on deep-reactive ion etching processed by Microfluidic Foundry company. To transfer both the full and partial etching patterns, two photomasks are used. The silicon wafer is first prepared with a buried oxide layer. Subsequently, the dioxide layer is removed for the partial etching regions. Next, the photoresist is employed to transfer the pattern for full etching. After full etching, followed by the removal of the photoresist, partial etching is processed for the region uncovered with the oxide layer. After that, the oxide layer is removed from the device.

Figure 4(a) shows pictures of the fabricated OAM emitters for OAM +1/–1 and OAM +1/–2. The scanning electron microscopy (SEM) pictures of the tapering structure, effective medium cladding, and OAM converter are presented in Figs. 4(b, c). Note that while the fabrication resolution of the transferred transverse patterns is relatively high, the depth fluctuations for partial etching could shift the center frequency of the device, influencing the device bandwidth, and inducing higher emission loss [41].

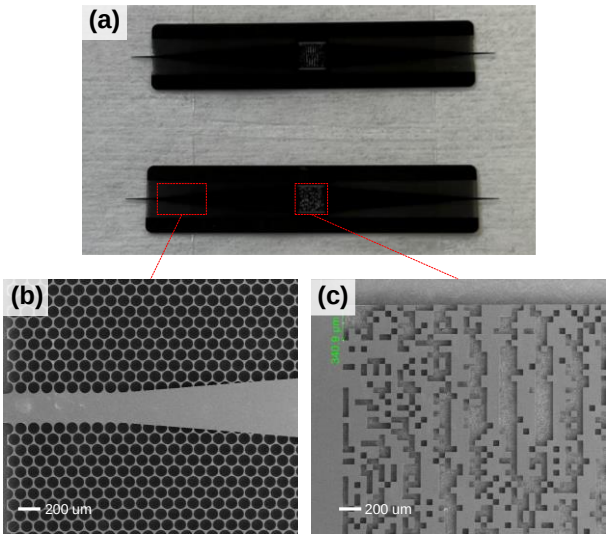

Fig. 4. (a) Pictures of the THz integrated OAM emitter for OAM +1 and –1 (top) and OAM +1 and –2 (bottom). (b, c) Scanning electron microscopy pictures of the fabricated device.

III. EXPERIMENTAL RESULTS

The experimental setup for the characterization of the generated OAM mode and data transmission is shown in Fig. 5(a). At the transmitter, the output of Laser 1 is modulated with a 5-Gbaud QPSK signal using an in-phase and quadrature (I/Q) modulator. After being amplified by an erbium-doped fiber amplifier (EDFA), the data-carrying signal is combined with continuous-wave (CW) light from Laser 2 using a 3-dB coupler. The frequency spacing between the two lasers controls the carrier frequency of the generated THz signal $f_{THz} = \Delta f$, and is set to be ~300 GHz. The polarizations of Laser 1 and Laser 2 are aligned utilizing polarization controllers (PCs).

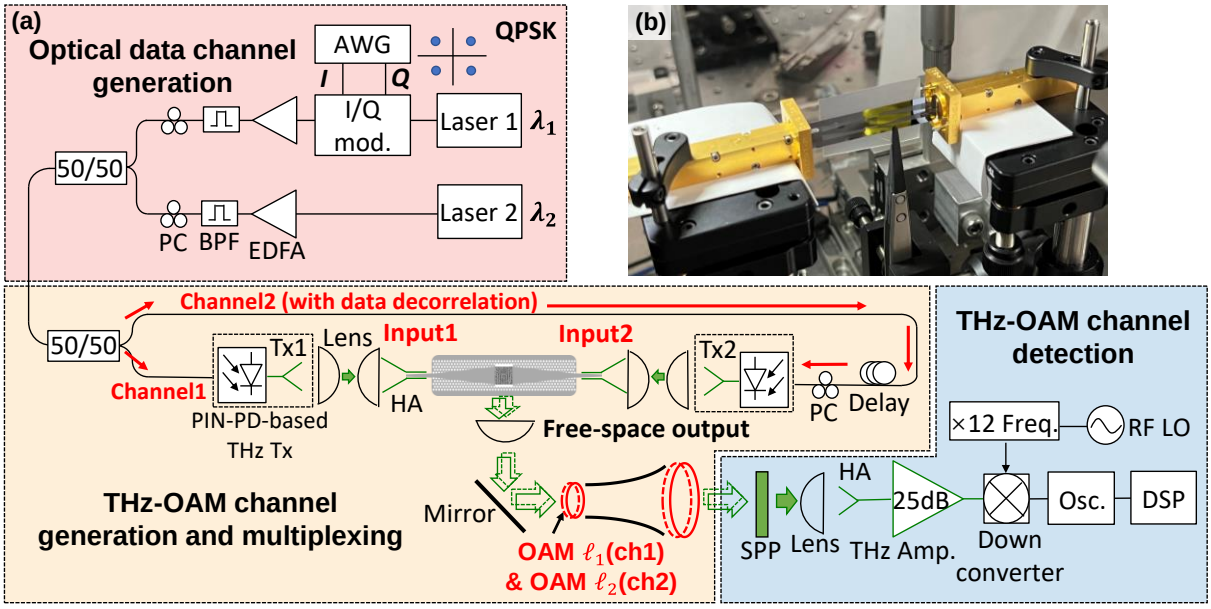

Fig. 5. (a) Experimental setup for characterizing the pixel-array-based THz integrated OAM emitter. A 20-Gbit QPSK THz OAM-multiplexed link, using two OAM beams generated and multiplexed at 0.315 THz, is achieved by using the integrated emitter. AWG: arbitrary waveform generator; EDFA: erbium-doped fiber amplifier; BPF: band pass filter; PC: polarization controller; SPP: spiral phase plate; HA: horn antenna (connected with hollow metallic waveguide); Osc.: oscilloscope; DSP: digital signal processing.

Subsequently, the combined signal is split into two paths, and one of the paths is delayed by a 15-m fiber for data decorrelation. For each path, the combined data signal and CW light are mixed in a positive-intrinsic-negative photodiode-based (PIN-PD-based) THz Gaussian transmitter to generate a THz data signal in free space. The free-space THz signal is directly coupled into two WR3.4 metallic waveguides by polytetrafluoroethylene (PTFE) lenses (50 mm diameter and 75 mm focal length) and horn antennas (HA). The THz integrated circuit is inserted into metallic waveguides to generate two coaxially propagating OAM beams with different OAM orders regarding different inputs from different waveguides. Fig. 5(b) shows a picture of the integrated device inserted into the metallic waveguides. The generated beams are collimated by the same type of PTFE lens. For single-generated mode characterization, the I/Q modulator is bypassed, so CW THz OAM beams are emitted from the device without carrying data.

At the receiver, after a transmission distance of ~ 25 cm, the multiplexed OAM beams are converted back to a Gaussian beam, one at a time using a spiral phase plate [14]. The SPPs are fabricated from high-density polyethylene (HDPE) through computer numerical control milling techniques. The back-converted THz beam is focused by a PTFE lens and collected by a HA, subsequently amplified by a THz amplifier, and down-converted to an intermediate frequency (IF) band by beating with a 12-times frequency multiplied radio frequency (RF) signal from the electrical local-oscillator (LO) in a THz sub-harmonic down converter ($f_{IF} = f_{THz} - 12 \times f_{LO}$). The IF signal is sampled by a digital oscilloscope and demodulated by offline processing. In our demonstration, we recover a single THz data channel at a time. Simultaneously receiving multiple multiplexed OAM modes can be achieved by using multiple beam splitters, SPPs for corresponding modes, and THz receivers. However, in this scheme, if the number of multiplexed modes increases, a cascade of beam splitters will lead to higher splitting loss.

Moreover, the THz integrated OAM emitter could also be potentially used as an OAM demultiplexer and receiver [49], [50]. Accordingly, similar mode conversion efficiency and crosstalk would be expected for an integrated receiver. If the integrated mode converters are used as both the transmitter and receiver, the link loss and channel crosstalk could depend on the mode conversion efficiency, modal purity of the mode converter, beam divergence of OAM modes, and misalignment between the transmitter and the receiver. Additionally, to maximize the mode conversion efficiency and reduce the modal crosstalk as a receiver, the proper alignment and focus of the received beam might be required to match the modal field of the integrated mode converter [49], [50].

A. Characterization of the generated OAM modes

To characterize the generated OAM beams emitted from the THz integrated OAM emitter, we first transmit a CW THz wave and measure the intensity profile of the generated OAM beams. The interferogram of the OAM beam with a Gaussian beam is also measured. To obtain these profiles, the THz receiver is attached to a two-dimensional translation stage to scan the profile. The output IF power is recorded by an electrical spectrum analyzer. The resolution of the scanning process is 0.75 mm, and the profile size is 30 mm. The center frequency is also characterized, and it is ~0.317 THz for the OAM +1/–1 emitter, and ~0.319 THz for the OAM +1/–2 emitter, potentially due to the depth fluctuations. As shown in Fig. 6, the generated OAM modes have a ring-shaped intensity profile. The diameter of the OAM ±1 beams is ~ 13 mm, and the diameter of the OAM –2 beams is ~ 16 mm. The results indicate that higher-order OAM modes tend to be more distorted in the modal profiles. The potential reasons are illustrated in Section II.

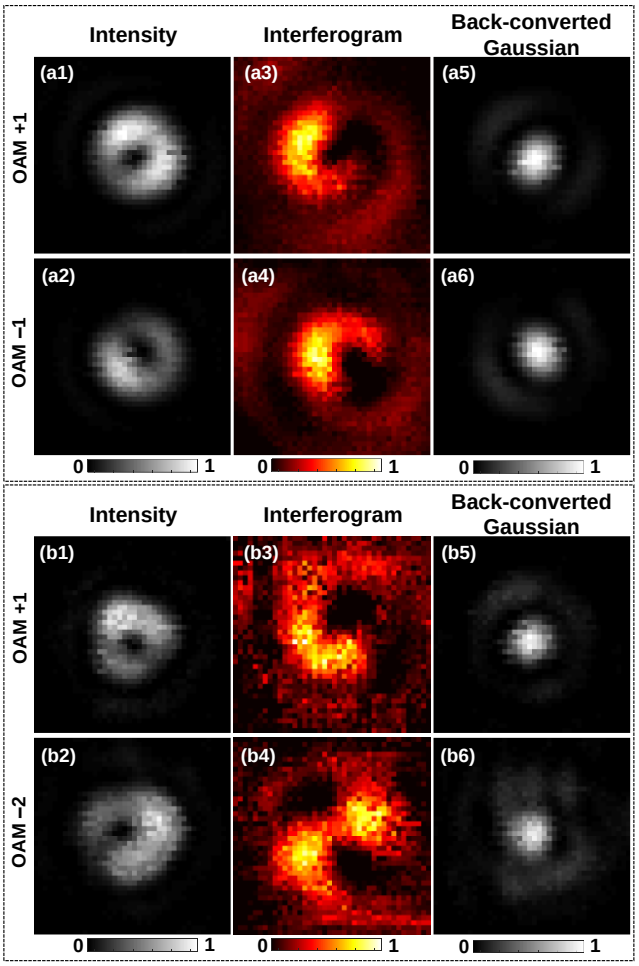

Fig. 6. (a1, a2, b1, b2) Intensity profiles, (a3, a4, b3, b4) interferogram with a THz Gaussian beam, and (a5, a6, b5, b6) back-converted Gaussian beam for the generated OAM +1/–1 and OAM +1/–2 by two THz-integrated OAM emitters.

To measure the interferogram, with the input THz power from one coupling spike, the power leaked to the other coupling spike can be used as a coherent copy. In the experiment, we insert a mirror between the lens and the PIN-PD-based THz transmitter on the other side, thus, the THz from that HA will generate a Gaussian beam that is coherent with the OAM beam generated by the integrated emitter. Beam splitters and mirrors are used to combine the OAM beam and the Gaussian beam. A simplified setup for measuring the interferogram of the generated OAM beam from the left port is shown in Fig. 7. The number of rotating arms and the rotating direction (clockwise or counterclockwise direction) shown in the interferograms

correspond to the mode order of the relevant OAM beams and their signs. The intensity profiles of back-converted Gaussian beams are also investigated using corresponding SPPs to convert the OAM beams back to the Gaussian beams, as shown in Figs. 6(a5, a6, b5, b6).

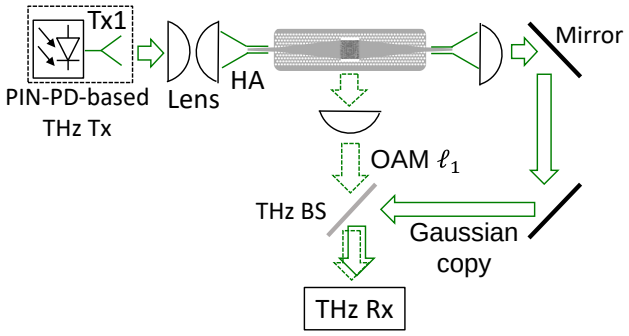

Fig. 7. Experimental setup for measuring the interferogram of an OAM beam with a Gaussian beam. BS: beam splitter; HA: horn antenna.

We also measure the modal spectra of the generated OAM beams to evaluate the modal purities, as shown in Fig. 8. The power distribution of receiving different OAM modes is recorded by changing the OAM order of the SPP at Rx. Taking the OAM +1/–1 emitter as an example, the power leaked to the neighboring modes is ~ –11 dB and ~ –9 dB for OAM +1 and –1, respectively. The resulting modal spectra in Fig. 8 should be viewed only as approximate ones since fabrication-related imperfections in the SPPs themselves make them non-ideal mode converters.

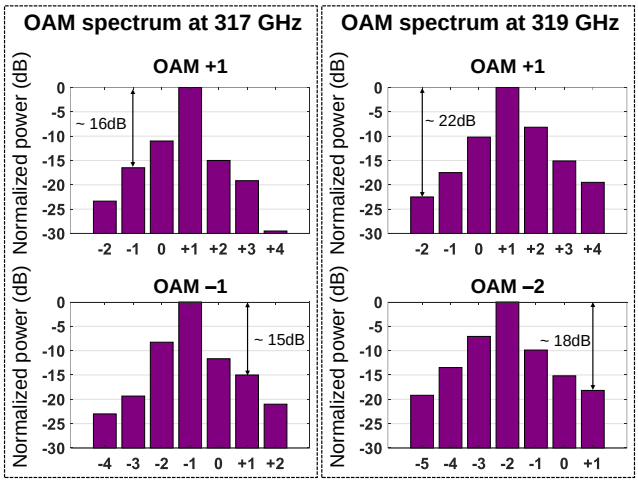

Fig. 8. Modal spectra for OAM +1/–1 and OAM +1/–2 beams at the center frequency of the device ~317 GHz and ~319 GHz.

B. *Characterization of the THz OAM-multiplexed link*

In our experiment, we choose the THz integrated OAM +1/–1 emitter as an example to demonstrate a THz OAM-multiplexed link. We first measure the normalized received power of two multiplexed OAM +1/–1 channels. In our experiment, we measure the power ratio of the transmitted THz power from the THz emitter to the free-space THz power before the THz receiver as the total link loss. At 317 GHz, the link loss is estimated to be ~8 dB and ~9.5 dB for the OAM +1 and OAM –1 modes, respectively. This link loss mainly could be caused by the insertion loss of the integrated OAM emitter. In our proof-of-concept characterization, the propagation loss is relatively low for a ~25-cm link distance.

The results in Fig. 9(a) show a ~ –16-dB modal crosstalk between OAM +1 and OAM –1 at 317 GHz. Furthermore, with a similar approach, we measure the received power of OAM +1/–1 modes when transmitting OAM +1/–1 at different frequencies to characterize the bandwidth of the device. Figure 9(b) represents a relative 3-dB power bandwidth of ~15 GHz for the integrated OAM emitter, and the crosstalk between OAM +1/–1 channels remains <–10 dB within this band. The insertion loss and crosstalk are frequency dependent and that could be because the phase delay generated by the mode converter varies for different frequencies. Moreover, to accommodate the limited power budget in an opto-electronic THz system, the insertion loss could be potentially improved by (i) optimizing the partial-etch depth to increase the mode conversion efficiency [41], and (ii) adding a backside reflector under the silicon device [41].

In addition, as mentioned above, the imperfection and bandwidth of the SPP may affect the bandwidth measurement, especially since the SPPs show a frequency dependent degradation [14]. Compared with the simulation, we note a frequency shift of the frequency center of the device, as well as a decrease in the bandwidth. This could be due to fluctuations in the depth of partially etched pixels influencing the center frequency of the device mentioned in Section II. Subsequently, the mismatch of the center frequency degrades the device bandwidth.

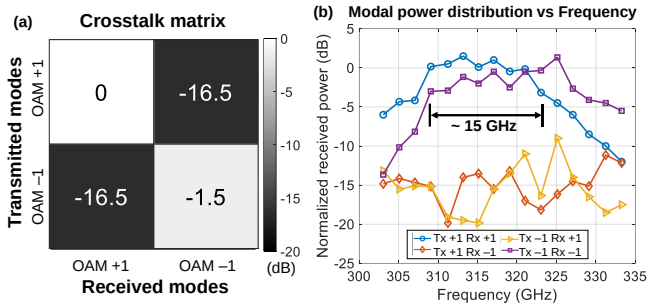

Fig. 9. (a) Channel crosstalk between two multiplexed OAM channels generated by the THz integrated emitter. (b) Modal power distribution at different frequencies ranging from 303 GHz to 333 GHz.

We further demonstrate a 20-Gbit/s QPSK THz wireless link multiplexing OAM +1 and OAM –1, where each channel carries a 5-Gbaud signal using the integrated OAM emitter. Figures 10(a, b) show the optical spectra at Tx and the electrical spectra after down-conversion to ~11.6 GHz at the Rx. The LO frequency is set to 25.45 GHz. Therefore, the THz frequency is estimated to be ~ 317 GHz. Figure 10(c) shows the bit error rate (BER) performance of the OAM +1/–1 channels at different SNRs with single-OAM channels or multiplexed-OAM ones. In the experiment, we set different input optical powers at Tx to change the received IF power level to vary the SNR. The SNR values are estimated from the IF spectrum of the received signal. For the THz OAM-multiplexed link, the crosstalk from different OAM data-carrying channels induces ~1 dB SNR penalties at the BER of 3.8×10-3. The corresponding constellations and measured error vector magnitudes (EVMs)

for single or multiplexed data channels at an SNR ~11 dB are shown in Fig. 10(d). Compared to single-channel transmission, the constellation diagrams become more blurred, and the EVMs increase as a result of the inter-channel crosstalk between the OAM +1 and –1 channels.

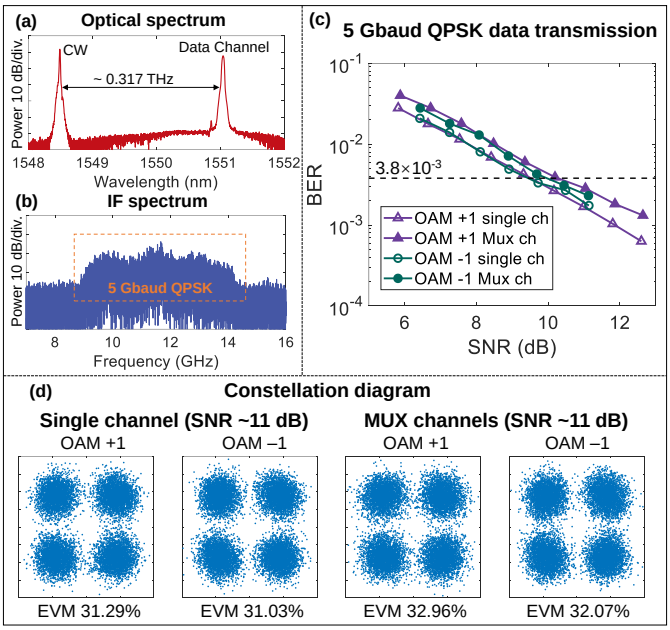

Fig. 10. (a) Optical spectrum at the THz transmitter. (b) Electrical spectrum after down-conversion at the receiver. (c) Measured BER as a function of SNR for two multiplexed OAM channels with a 5-Gbaud QPSK signal. (d) The EVMs and constellation diagrams under an SNR of ~11 dB.

We note that the THz OAM +1/–2 mode converter could also potentially be used to multiplex OAM +1 and OAM –2 channels. Compared to the OAM +1/–1 emitter, it would be expected that: (a) the channel crosstalk between the OAM +1 and –2 modes tends to be lower as the mode separation spacing is larger, and (b) the received signal power tends to be lower as the mode conversion efficiency for higher-order modes is lower.

IV. Summary

In this paper, we have presented the design and fabrication of THz-integrated OAM emitters to generate and multiplex different data-carrying OAM beams. The generated OAM beams are experimentally characterized by two fabricated OAM emitters for generating OAM +1/–1 and OAM +1/–2. Crosstalk between the OAM modes of lower than < –15 dB is achieved. Furthermore, a 20-Gbit/s QPSK free-space THz link at 0.317 THz is experimentally demonstrated by multiplexing OAM +1 and –1, using the integrated circuit. Compared to a single-beam transmission, the multiplexed link induced a ~1-dB SNR penalty.

References

[1] S. Jia *et al.*, "THz photonic wireless links with 16-QAM modulation in the 375-450 GHz band," *Opt. Express*, vol. 24, no. 21, pp. 23777–23783, Oct. 2016.

[2] T. Nagatsuma, G. Ducournau, and C. C. Renaud, "Advances in terahertz communications accelerated by photonics," *Nat. Photonics*, vol. 10, no. 6, pp. 371–379, Jun. 2016.

[3] K. Su, L. Moeller, R. B. Barat, and J. F. Federici, "Experimental comparison of terahertz and infrared data signal attenuation in dust clouds," *J. Opt. Soc. Am. A*, vol. 29, no. 11, pp. 2360–2366, Nov. 2012.

[4] H. Elayan, O. Amin, B. Shihada, R. M. Shubair, and M.-S. Alouini, "Terahertz band: The last piece of RF spectrum puzzle for communication systems," *IEEE Open J.Commun. Soc.*, vol. 1, pp. 1–32, Nov. 2020.

[5] T. Nagatsuma *et al.*, "Terahertz wireless communications based on photonics technologies," *Opt. Express*, vol. 21, no. 20, pp. 23736–23747, Oct. 2013.

[6] S. Koenig *et al.*, "Wireless sub-THz communication system with high data rate," *Nat. Photonics*, vol. 7, no. 12, pp. 977–981, Dec. 2013.

[7] T. Harter *et al.*, "Generalized Kramers–Kronig receiver for coherent terahertz communications," *Nat. Photonics*, vol. 14, no. 10, pp. 601–606, Oct. 2020.

[8] X. Pang *et al.*, "Bridging the terahertz gap: photonics-assisted free-space communications from the submillimeter-wave to the mid-infrared," *J. Lightwave Technol.*, vol. 40, no. 10, pp. 3149–3162, Feb. 2022.

[9] L. Zhang, X. Pang, S. Jia, S. Wang, and X. Yu, "Beyond 100 Gb/s optoelectronic terahertz communications: key technologies and directions," *IEEE Communications Magazine*, vol. 58, no. 11, pp. 34–40, Nov. 2020.

[10] S. Jia *et al.*, "Integrated dual-laser photonic chip for high-purity carrier generation enabling ultrafast terahertz wireless communications," *Nat. Commun.*, vol. 13, no. 1, Mar. 2022.

[11] R. Shrestha, H. Guerboukha, Z. Fang, E. Knightly, and D. M. Mittleman, "Jamming a terahertz wireless link," *Nat. Commun.*, vol. 13, no. 1, Jun. 2022.

[12] T. Kürner, D. M. Mittleman, and T. Nagatsuma, Eds., *THz Communications*. Springer International Publishing, 2022.

[13] H. Tataria, M. Shafi, A. F. Molisch, M. Dohler, H. Sjöland, and F. Tufvesson, "6G wireless systems: vision, requirements, challenges, insights, and opportunities," *Proceedings of the IEEE*, vol. 109, no. 7, pp. 1166–1199, Jul. 2021.

[14] H. Zhou *et al.*, "Utilizing multiplexing of structured THz beams carrying orbital-angular-momentum for high-capacity communications," *Opt. Express*, vol. 30, no. 14, pp. 25418–25432, Jul. 2022.

[15] Y. Yan *et al.*, "High-capacity millimetre-wave communications with orbital angular momentum multiplexing," *Nat. Commun.*, vol. 5, no. 1, Sep. 2014.

[16] J. Wang *et al.*, "Terabit free-space data transmission employing orbital angular momentum multiplexing," *Nat. Photonics*, vol. 6, no. 7, pp. 488–496, Jul. 2012.

[17] A. M. Yao and M. J. Padgett, "Orbital angular momentum: origins, behavior and applications," *Adv. Opt. Photon.*, vol. 3, no. 2, pp. 161–204, Jun. 2011.

[18] L. Allen, M. W. Beijersbergen, R. J. C. Spreeuw, and J. P. Woerdman, "Orbital angular momentum of light and the transformation of Laguerre-Gaussian laser modes," *Phys. Rev. A*, vol. 45, no. 11, pp. 8185–8189, Jun. 1992.

[19] M. Smit, J. van der Tol, and M. Hill, "Moore's law in photonics," *Laser & Photonics Reviews*, vol. 6, no. 1, pp. 1–13, Sep. 2012.

[20] K. Sengupta, T. Nagatsuma, and D. M. Mittleman, "Terahertz integrated electronic and hybrid electronic–photonic systems," *Nat. Electron.*, vol. 1, no. 12, pp. 622–635, Dec. 2018.

[21] Y. Yang *et al.*, "Terahertz topological photonics for on-chip communication," *Nat. Photonics*, vol. 14, no. 7, pp. 446–451, Jul. 2020.

[22] R. A. S. D. Koala, M. Fujita, and T. Nagatsuma, "Nanophotonics-inspired all-silicon waveguide platforms for terahertz integrated systems," *Nanophotonics*, vol. 11, no. 9, pp. 1741–1759, Apr. 2022.

[23] D. Headland, W. Withayachumnankul, M. Fujita, and T. Nagatsuma, "Gratingless integrated tunneling multiplexer for terahertz waves," *Optica*, vol. 8, no. 5, pp. 621–629, May 2021.

[24] C. Zheng *et al.*, "All-dielectric metasurface for manipulating the superpositions of orbital angular momentum via spin-decoupling," *Advanced Optical Materials*, vol. 9, no. 10, p. 2002007, Mar. 2021.

[25] X. Zang *et al.*, "Manipulating terahertz plasmonic vortex based on geometric and dynamic phase," *Advanced Optical Materials*, vol. 7, no. 3, p. 1801328, Dec. 2019.

[26] R. Dharmavarapu *et al.*, "Dielectric cross-shaped-resonator-based metasurface for vortex beam generation at mid-IR and THz wavelengths," *Nanophotonics*, vol. 8, no. 7, pp. 1263–1270, Jul. 2019.

[27] X. Zang *et al.*, "Metasurfaces for manipulating terahertz waves," *Light: Advanced Manufacturing*, vol. 2, no. 2, pp. 148–172, Jun. 2021.
[28] M. I. W. Khan *et al.*, "A 0.31-THz orbital-angular-momentum (OAM) wave transceiver in CMOS with bits-to-OAM mode mapping," *IEEE J. of Solid-State Circuits*, vol. 57, no. 5, pp. 1344–1357, Dec. 2022.
[29] X. Su *et al.*, "THz integrated circuit with a pixel array to multiplex two 10-Gbit/s QPSK channels each on a different OAM beam for mode-division-multiplexing," in *Optical Fiber Communication Conference (OFC) 2022, paper Th4B.4*, Mar. 2022.
[30] Z. Xie *et al.*, "Ultra-broadband on-chip twisted light emitter for optical communications," *Light Sci Appl*, vol. 7, no. 4, p. 18001, Apr. 2018.
[31] D. Headland, W. Withayachumnankul, X. Yu, M. Fujita, and T. Nagatsuma, "Unclad microphotonics for Terahertz waveguides and systems," *J. Lightwave Technol.*, vol. 38, no. 24, pp. 6853–6862, Dec. 2020.
[32] B. Shen, P. Wang, R. Polson, and R. Menon, "An integrated-nanophotonics polarization beamsplitter with 2.4×2.4 μm^2 footprint," *Nat. Photonics*, vol. 9, no. 6, pp. 378–382, Jun. 2015.
[33] Y. Li *et al.*, "Orbital angular momentum multiplexing and demultiplexing by a single metasurface," *Advanced Optical Materials*, vol. 5, no. 2, p. 1600502, Nov. 2017.
[34] R. C. Devlin, A. Ambrosio, N. A. Rubin, J. P. B. Mueller, and F. Capasso, "Arbitrary spin-to–orbital angular momentum conversion of light," *Science*, vol. 358, no. 6365, pp. 896–901, Nov. 2017.
[35] N. Yu and F. Capasso, "Flat optics with designer metasurfaces," *Nat. Mater.*, vol. 13, no. 2, pp. 139–151, Feb. 2014.
[36] A. Liu *et al.*, "On-chip generation of the reconfigurable orbital angular momentum with high order," *Opt. Express*, vol. 28, no. 12, pp. 17957–17965, Jun. 2020.
[37] C. M. Lalau-Keraly, S. Bhargava, O. D. Miller, and E. Yablonovitch, "Adjoint shape optimization applied to electromagnetic design," *Opt. Express*, vol. 21, no. 18, pp. 21693–21701, Sep. 2013.
[38] A. Y. Piggott, J. Lu, K. G. Lagoudakis, J. Petykiewicz, T. M. Babinec, and J. Vučković, "Inverse design and demonstration of a compact and broadband on-chip wavelength demultiplexer," *Nat. Photonics*, vol. 9, no. 6, pp. 374–377, Jun. 2015.
[39] S. Molesky, Z. Lin, A. Y. Piggott, W. Jin, J. Vucković, and A. W. Rodriguez, "Inverse design in nanophotonics," *Nat. Photonics*, vol. 12, no. 11, pp.659–670, Nov. 2018.
[40] A. D. White *et al.*, "Gradient-based optimization of optical vortex beam emitters." arXiv, Feb. 18, 2022.
[41] N. Zhou *et al.*, "Ultra-compact broadband polarization diversity orbital angular momentum generator with 3.6×3.6 μm^2 footprint," *Science Advances*, vol. 5, no. 5, p. 9593, May 2019.
[42] H. Guan *et al.*, "Compact and low loss 90° optical hybrid on a silicon-on-insulator platform," *Opt. Express*, vol. 25, no. 23, pp. 28957–28968, Nov. 2017.
[43] Y. Liu, L. Søgaard Rishøj, M. Galili, Y. Ding, L. K. Oxenløwe, and T. Morioka, "Data transmission using Orbital Angular Momentum mode multiplexing and wavelength division multiplexing with a silicon photonic integrated MUX chip," in *2021 European Conference on Optical Communication (ECOC)*, pp. 1–4, Sep. 2021.
[44] H. Song *et al.*, "Demonstration of generating a 100 Gbit/s orbital-angular-momentum beam with a tunable mode order over a range of wavelengths using an integrated broadband pixel-array structure," *Opt. Lett.*, vol. 46, no. 19, pp. 4765–4768, Oct. 2021.
[45] H. Song *et al.*, "Experimental demonstration of generating a 10-Gbit/s QPSK Laguerre-Gaussian beam using integrated circular antenna arrays to tune both spatial indices," in *Conference on Lasers and Electro-Optics (2022)*, pp. 1–2, May 2022.
[46] C. Shirpurkar *et al.*, "Photonic crystal resonators for inverse-designed multi-dimensional optical interconnects," *Opt. Lett.*, vol. 47, no. 12, pp. 3063–3066, Jun. 2022.
[47] A. M. J. Koonen, H. Chen, H. P. A. van den Boom, and O. Raz, "Silicon photonic integrated mode multiplexer and demultiplexer," *IEEE Photon. Technol. Lett.*, vol. 24, no. 21, pp. 1961–1964, 2012.
[48] M. Zhang, H. Liu, B. Wang, G. Li, and L. Zhang, "Efficient grating couplers for space division multiplexing applications," *IEEE J. Sel. Top. Quantum Electron.*, vol. 24, no. 6, pp. 1–5, 2018.
[49] S. Li *et al.*, "Orbital angular momentum vector modes (de)multiplexer based on multimode micro-ring," *Opt. Express*, vol. 26, no. 23, pp. 29895–29905, Nov. 2018.
[50] H. Song *et al.*, "Demonstration of recovering orbital-angular-momentum multiplexed channels using a tunable, broadband pixel-array-based photonic-integrated-circuit receiver," *J. Lightwave Technol.*, vol. 40, no. 5, pp. 1346–1352, Mar. 2022.